Iranian Journal of Materials Forming

Research Article

Hot Workability and Processing Map of High Gd Content Mg-Gd-Zn-Zr-Nd Alloy

S. Mosadegh[1], M. Aghaie-Khafri[1*] and B. Binesh[2]

[1] Faculty of Materials Science and Engineering, K. N. Toosi University of Technology, Tehran, Iran
[2] Department of Materials Science and Engineering, University of Bonab, Bonab, Iran

A R T I C L E   I N F O

A B S T R A C T

Hot workability of as-extruded high Gd content Mg-5Gd-0,5Zn-0.5Zr-2.5Nd alloy was investigated using the hot compression test in a temperature range of 300-500 °C and strain rates of 0.001-1s⁻¹. Hot workability assessment was conducted by capturing microstructural evolution of high temperature deformed samples, and by constructing power dissipation and instability maps. Using experimental data of hot compression tests, the power dissipation map of the alloy was constructed, in which a domain of dynamic recrystallization (DRX) occurred at the temperature range of 350-450 °C and strain rate of $0.001\text{-}0.1$ s⁻¹, representing the optimum hot working window. Furthermore, the processing map of the alloy was constructed, and flow instability regions were also indicated based on the Ziegler's flow instability criterion.

1. Introduction

Magnesium is the lightest structural metal and appears as a hexagonal lattice structure [1]. Mg-alloys are a popular candidate used to fabricate different components in automotive and aerospace industries because of their superior physical and mechanical properties [2-5]. Considering the low ductility of Mg alloys at room temperature, the deformation process is almost performed at elevated temperatures [6]. Deformation at high temperatures improves the formability of the Mg alloys, and can affect the size, density, and morphology of the precipitates [7]. The common method for the shaping of the Mg alloys is hot extrusion [6].

Alloying elements in Mg-alloys mainly improves the corrosion resistance and mechanical properties of the Mg based components. The Mg-rare earth (RE) systems have attracted great interest because RE additions can improve both the formability and the strength of Mg alloys through the solid solution strengthening and precipitation hardening mechanisms [8, 9].

Among different alloying elements, Gd is considered as one of the most effective ones to improve the high performance of Mg-alloys [10]. This is caused as a result of the fact that at high temperatures, the solubility of Gd and Y in Mg increases, significantly (12.47 wt.% at 566°C and 23.89 wt.% at 540°C for Gd), and the alloy exhibits less solubility at room and intermediate temperatures [11]. Kula et al. [12] reported that the Mg-Gd alloys exhibit superior strength and ductility under tension and compression, which was one of the consequences of the more effective solid solution strengthening and grain-boundary strengthening.

Moreover, the addition of transition elements such as Zn and Zr to Mg-alloys could result in developing the age hardening [13]. Zr, a grain refiner agent, was added to Mg alloys to achieve a fine-grained microstructure and improve the mechanical properties [14]. Wang et al. observed a strong age hardening effect following the T6 heat treatment of the Mg-Gd-Y-Zr alloy [15]. According to Honma et al. [16], although the addition of Zn to Mg-Gd-Y-Zr alloy degraded the age-hardening response; however, long period stacking ordered (LPSO) phases were formed at the grain boundaries and within the grains which improved the maximum tensile elongation.

In the recent years, a comprehensive study has been done on the creep resistance behavior and age hardening response of as-cast and as-extruded Mg-Sn based alloys [17-19]. Xiaoping Luo et al. [20] investigated high-temperature deformation behaviors of the as-cast Mg-Sn-Y-Zr alloy at 250 to 450°C and 0.002 to 2s^{-1} strain rates. They proposed that the apparent activation energy of the as-cast Mg-Sn-Y-Zr alloy was 223.26 kJ /mol. Park et al. [21] showed that Mg-8Al-4Sn-2Zn alloys exhibit greater tensile strength and elongation in comparison with Mg-8Al-0.5Zn alloys.

Many studies have been conducted to enhance the mechanical properties of Mg-RE alloys by hot extrusion and heat treatment [22]. Honma et al. [16] developed a high-strength and ductile Mg-10Gd-5.7Y-1.6Zn-0.5Zr (wt.%) alloy prepared by the hot extrusion and subsequent aging. The alloy exhibited a tensile yield strength of 473 MPa and elongation of 80%. Investigation of Jin et al. [23] on Mg-Gd-Y-Zn-Zr magnesium alloy showed that some eutectic phases in the cast alloy dissolved into the matrix following the high temperature extrusion. Heng et al. [24] developed a super high-strength Mg-Gd-Y-Zn-Mn alloy by using hot extrusion and strain aging. They suggested that hot extrusion and strain aging, especially where cold rolling plus stretching was applied before aging, is an effective approach for developing high-strength Mg alloys.

As one of the newly developed Mg-Gd alloys, Mg-Gd-Nd-Zn-Zr exhibits excellent mechanical properties and biocorrosion resistance [25]. Despite some researches conducted on the Mg-Gd-Nd-Zn-Zr, a small number of them have focused on the hot deformation of the alloys [26]. To achieve the optimum hot deformation parameters of high Gd content Mg-Gd-Zn-Zr-Nd alloy, stress-strain curves and processing map of the homogenized and extruded Mg-5Gd-0.5Zn-0.5Zr-2.5Nd alloy were studied in this work.

2. Experimental Procedure
2.1. Casting and hot working

The ingot of Mg-5Gd-2.5Nd-0.5Zn-0.5Zr alloy was made by melting Mg-90% Gd, Mg-25%Nd, and Mg-30%Zr master alloys, commercially pure Mg (>99.95%), and Zn (>99.95%). The starting material was melted in an electrical resistance furnace at 750±3 °C, where a mixed atmosphere of CO_2 and SF_6 with the ratio of 99:1 was applied. Following the cooling of the melt to 730±3 °C, it was poured into a steel mold which had been preheated to 200±3 °C. Chemical composition of the cast material obtained by the inductively coupled plasma (ICP) method is listed in Table 1.

Table 1. Chemical composition of the cast alloy in wt.%

Gd	Zn	Zr	Nd	Mg	Rest
5.23	0.56	0.47	2.54	91.17	0.03

The cast ingot was homogenized at 520±3 °C for 10 h. The homogenized ingot was machined to bars of 30 mm length and 30 mm diameter. Subsequently, the cast bars were extruded at 420 °C with an extrusion ratio of 1:6 and a ram speed of 0.1 mm s^{-1}.

2.2. Hot compression test

Extruded bars were machined into cylinders with a length of 12 mm and a diameter of 8 mm. Hot compression tests were performed using a Zwick Roell 250 testing machine (Zwick GmbH & Co. KG, Ulm, Germany), equipped with a fully computerized furnace. Different temperatures of 300 °C, 350 °C, 400 °C, 450 °C and 500 °C and strain rate ranges of 0.001 s^{-1}, 0.01 s^{-1}, 0.1 s^{-1}, and 1 s^{-1} were used. Following heating of the samples to the deformation temperature, they were held for 5 min before being compressed for uniform temperature distribution and to eliminate any thermal gradient. Samples hot deformed up to the true strain of 0.7 s^{-1}, and the specimens were immediately water quenched after compression to save the compressed microstructure.

The true stress-true strain curves were derived from the load-stoke data after eliminating the friction effect according to the following [27]:

$$\frac{P}{\sigma} = \left(\frac{h}{4\mu a}\right)^2 \left(e^{\frac{2\mu a}{h}} - \frac{2\mu a}{h} - 1\right) \tag{1}$$

where P is the uncorrected flow stress, σ is the corrected flow stress, h and a are instantaneous height and radius of the sample. μ is the friction coefficient that was calculated based on the barreling of each specimen [28].

2.3. Microstructure characterization

Samples for optical microscopy were mechanically polished by emery paper grade of 100 to 3000 followed by a diamond paste of 0.1, 0.5, and 0.25 μm, and then etched with a solution of 5ml acetic acid, 0.6 mg picric acids, 10 ml ethanol, and 10 ml DW.

Microstructures of the samples were characterized using a MF-AKS Zeiss optical microscope (OM), and ESEM Quanta 200 scanning electron microscope equipped with an energy dispersive spectrometer (EDS) system. The grain size was computed by using IMAGE J software, and based on the Hein's cross-sectional method, as per ASTME112 standards.

3. Results and Discussion
3.1. Stress-strain curve

Figure 1 shows the stress-strain curves of Mg-5Gd-0,5Zn-0.5Zr-2.5Nd alloy at 300 °C, 350 °C, 400 °C, 450 °C, 500 °C, and strain rates of 0.001, 0.01, 0.1, and 1 s^{-1}. It can be observed that flow stress was mainly increased by strain rate and decreased by temperature. A single peak flow curve is generally observed in which the flow stress generally increased due to the strain hardening until it reached a maximum value, followed by a dynamic softening, and finally attained the steady-state stress. The steady-state condition is established by a dynamic balance between strain hardening and strain softening. However, at 300 °C no steady-state condition was established as a consequence of limited workability and early fracture of the specimens. The observed dynamic softening, i.e., the single peak behavior can be ascribed to the dynamic recrystallization (DRX). The observed flow behavior is consistent with other investigations on Mg alloys [29-31].

It is interesting to note that the hot compression test specimen failed at 350 °C-1s^{-1} deformation condition. A similar failure of Mg-9Gd-4Y-0.6Zr and homogenized Mg-6.85Gd-4.52Y-1.15Nd-0.55Zr alloy was reported for deformation at 350 °C- 0.1, 1 s^{-1} and 350 °C-0.5, 5 s^{-1}, respectively [30, 31]. At low temperatures and high strain rates, the deformation mechanism changed from dislocation slip to twinning, cracks spread and ductility

decreased resulting in failure of the compression specimens [32].

Results obtained indicate that increasing temperatures and decreasing strain rates can accelerate the DRX kinetics. This is because higher temperatures result in faster diffusion, and smaller strain rates result in more time for nucleation and growth of recrystallized grains. Consequently, the strain hardening effect is decreased by increasing temperature and decreasing strain rate [33].
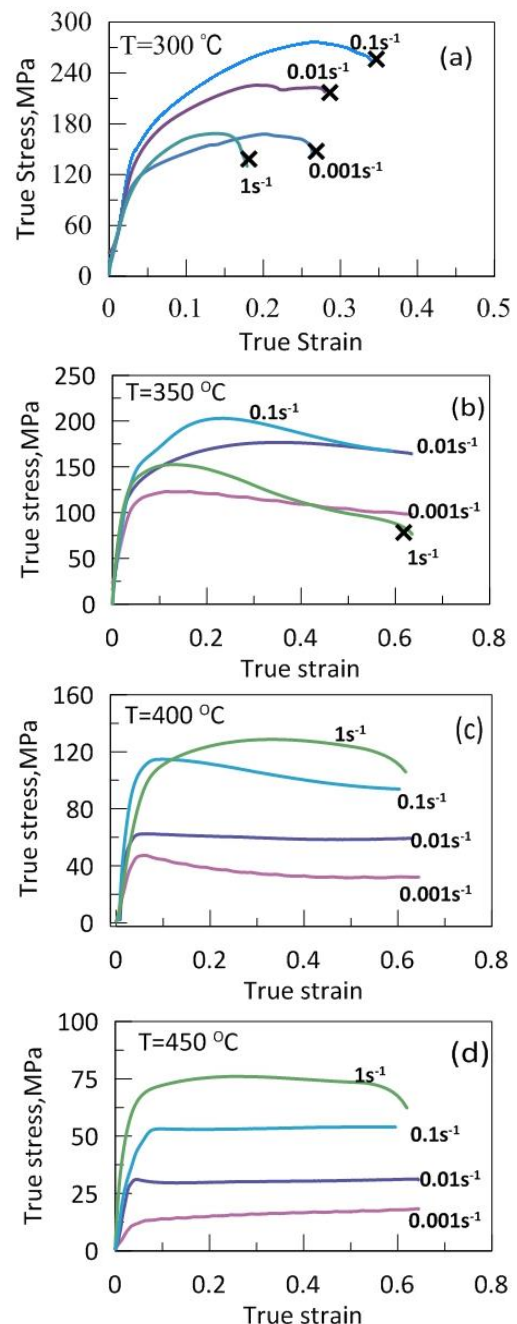

Fig. 1. True stress-strain curves for different temperatures and strain rates, (a) 300 °C, (b) 350 °C, (c) 400 °C, (d) 450 °C, and (e) 500 °C.
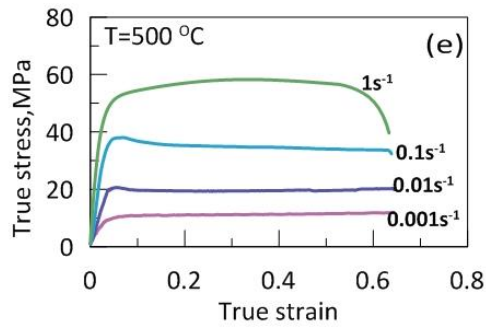
Fig. 1. Continue.

3.2. Grain size of hot deformed samples

Workability of hot deformed metals are highly dependent on the grain size and grain morphology. The microstructure of the specimen deformed at different temperatures and strain rates are almost equiaxed DRX grains. Fig. 2 shows the optical micrographs of samples deformed at 1 s^{-1} and different temperatures, in which typical DRX equiaxed grains are clearly observed.
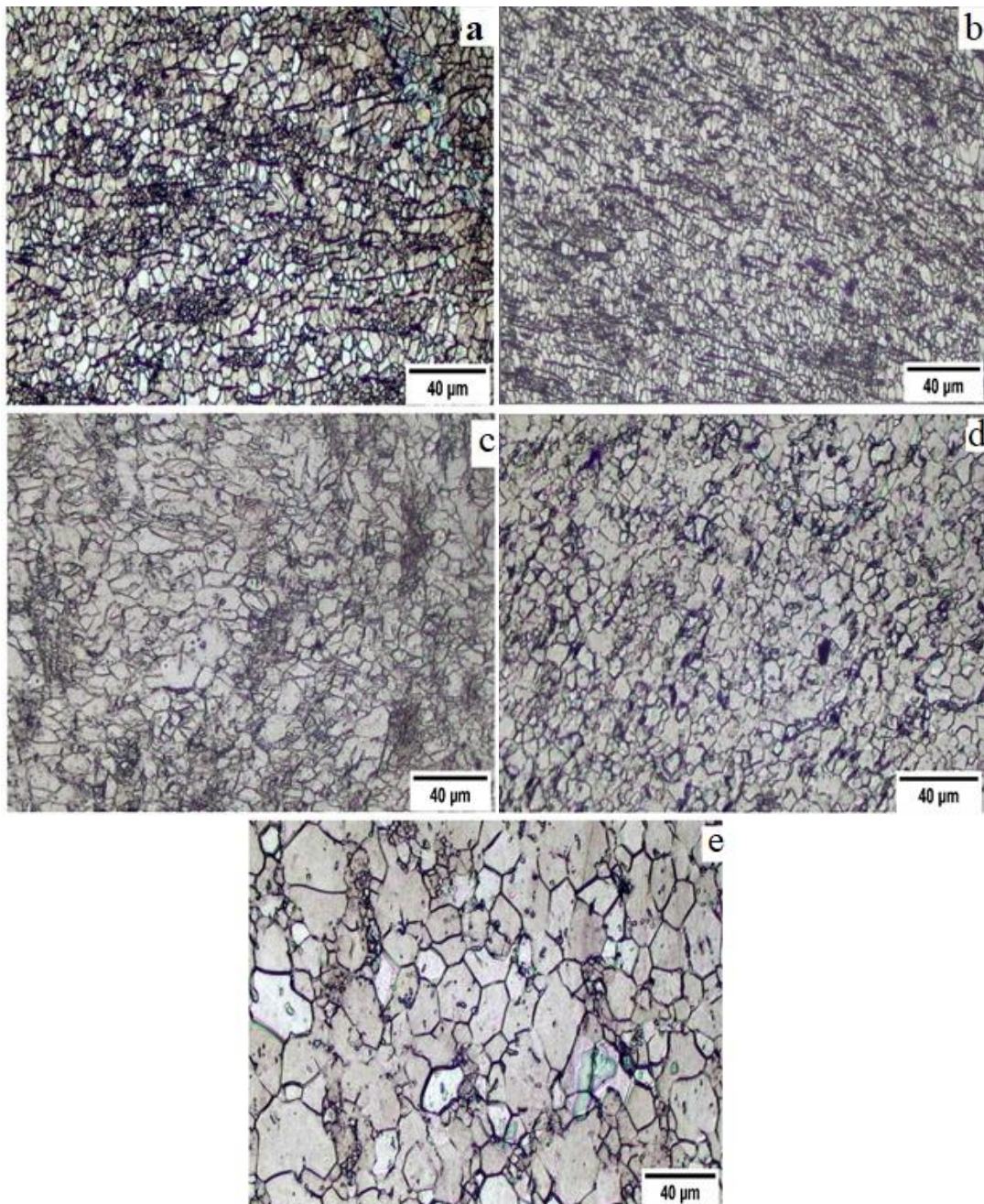

Fig. 2. Microstructure of samples hot deformed at strain rate of 1s^{-1} and (a) 300 °C, (b) 350 °C, (c) 400 °C, (d) 450 °C, and (e) 500 °C.

It is generally accepted that DRX gain size is highly dependent on the processing parameters, namely the Zener-Hollomon parameter [34]. The variation of DRX grain size with the Zener-Hollomon parameter for Mg-5Gd-2.5Nd-0.5Zn-0.5Zr alloy are shown in Fig. 3. The observed linear ln(D)-ln(Z) relationship can be expressed as $D = AZ^{-p}$, where, D is the grain size, and Z is the Zener-Hollomon parameter. The investigation by Barezban et al. [35] on the effect of Gd content on the pure Mg showed that the DRX grain size is dependent on Z, and decreases by the Gd content. Furthermore, the p value was constant and independent of the Gd, and A was dependent on the Gd percentage. In the present study, the mean values of p and A are 0.06 and $e^{5.02}$, respectively.
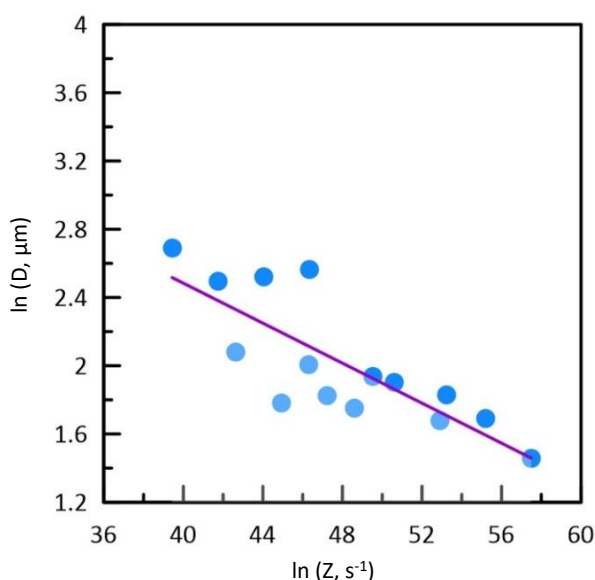

Fig. 3. DRX grain size dependence on the Z parameter.

The effect of deformation temperature and strain rate on the DRX grain size can be attributed to the dislocation density, dislocation mobility, and dislocation rearrangement. Increasing strain rate results in decreasing dislocation density and shorter time for dislocation rearrangement and sub-boundary movement which results in fine grain size. Furthermore, dislocation mobility increases with temperature and results in grain growth rate, and rough grain size. Besides, fine precipitates at the grain boundary, pins and render grain boundary movement, clearly shown in Fig. 2. Ebrahimi et al. [36] reported similar results on the precipitate pinning effect on the DRX grain boundary of AZ91 magnesium alloy, and the dominant effect of temperature on the grain size which is in accordance with the results of the present analysis.

3.3. Hot workability at low temperatures

Flow instabilities during the hot working occurred as a result of flow localization, kink and shear bands, flow rotations, mechanical twining, and dynamic strain aging [37]. If hard particles are present in a soft matrix, deformation causes the interface to crack and de-bond. The second common flow instability manifestation in the microstructure is flow localization. This is less intense than adiabatic shear band formation. Flow localization may also occur as a result of high strain rates [38].

Samples following deformation at different temperatures and strain rates are shown in Fig. 4, in which specimens deformed at 300 °C and different strain rates failed following imposing strain. Investigations on Mg-3.5Gd-1Zn-0.6Zr and Mg-6.5Gd-1.3Nd-0.7Y-0.3Zn alloys designated that deformation twins observed at 350 °C and lower temperatures [39, 40].

Non basal slip systems in Mg alloys are activated by increasing the deformation temperature and decreasing the strain rate. Prismatic and pyramidal slip systems in Mg alloys are activated above 200 °C and 300 °C, respectively [41]. It can be concluded that non-basal slip systems in Mg-5Gd-0.5Zn-0.5Zr-2.5Nd alloy are activated above 300 °C and enhance cross slipping and ductility. However, the observed low ductility in 300 °C is a result of few active slip systems, i.e. basal slip, at the imposed deformation temperature.

3.4. Construction of processing map

According to the dynamic material model, the workpiece under hot deformation conditions is assumed as a power dissipater. The system input energy (P) can be divided into two portions: G content and J co-content [42]. The total power is described as follows:

$$P = G + J = \int_0^{\dot{\varepsilon}} \sigma d\dot{\varepsilon} + \int_0^{\sigma} \dot{\varepsilon} d\sigma \qquad (2)$$

G is the dissipative energy of the material plastic deformation, most of which is converted into viscoplastic heat; the little remaining power is stored as lattice defects. J dissipater co-content represents the power dissipation by metallurgical mechanisms such as DRV, DRX, internal fracture (void formation or wedge cracking), superplastic flow, precipitation under dynamic conditions, and deformation-induced phase transformation.

$\dot{\varepsilon}(s^{-1})$	1	0.1	0.01	0.001
T=300 °C				
T=350 °C				
T=400 °C				
T=450 °C				
T=500 °C				

Fig. 4. Samples hot compressed at different temperatures and strain rates.

The power dissipated through microstructural processes is shown by a parameter called the efficiency of the power dissipation (η) [43], which is a dimensionless function of the strain rate sensitivity (m):

$$\eta = \left\{ 2\left[1 - \left(\frac{\frac{\sigma\dot{\varepsilon}}{(m+1)_{\dot{\varepsilon}_{min}}} + \int_{\dot{\varepsilon}_{min}}^{\dot{\varepsilon}} \sigma d\dot{\varepsilon}}{\sigma\dot{\varepsilon}} \right) \right] \right\} \frac{2m}{m+1} \tag{3}$$

The first equation can be considered for any stress and strain rate curves especially in the case of complicated alloy systems [44], but the latter equation is just used for alloys that have the power law behavior [45]. However, for materials in which the flow behavior does not obey the power law, Murty et al. [46] introduce a new efficiency of power dissipation as follows:

$$\eta = \frac{2J}{P} = 2\left(1 - \frac{G}{P} \right) \tag{4}$$

The power dissipation map is displayed by plotting iso-efficiency contours of η. The constructed power dissipation map for Mg-5Gd-2.5Nd-0.5Zn-0.5Zr alloy which is determined based on Eq. (4) is shown in Fig. 5. Three domains in the safe area with the peak efficiency of about 90%, 40%, and 30%, occur in the temperature and strain rate ranges of 300-350 °C/10^{-6}-1s^{-1} (domain A), 350-400 °C /10^{-6}-10^{-3}s^{-1} (domain B), and 350-500 °C 10^{-2}-1 s^{-1} (domain C), respectively. Typical efficiency for DRX in high stacking fault energy alloy is about 50%, and 30-40% for low stacking fault energy materials like Mg alloys. High efficiency of 60% is ascribed to the phenomenon such as cracking which is observed in the present study for samples deformed at 300 °C and different strain rates with the efficiency of 60-90%.
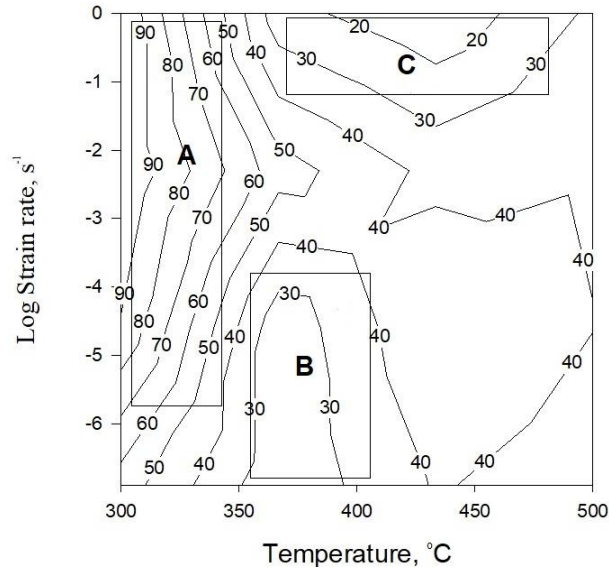
Fig. 5. The power dissipation map of Mg-5Gd-2.5Nd-0.5Zn-0.5Zr alloy, where contour numbers represent the percent efficiency of power dissipation; domain A: area under contour number 60 and vertical axes, domain B: area under contour number 40 and horizontal axes, domain C: area under contour number 30 and horizontal axes.

The representative microstructure in domains B and C (Figs. 6 and 7) reveals almost completely recrystallized structure with equiaxed DRX grains. Domain A with efficiency higher than 50% is an unstable region in which deformed samples were cracked. The microstructure corresponding to domain A (Figs. 8 and 9) indicates recrystallized structure, twins, and deformation bands, typically shown in Fig. 8. Furthermore, there are other contours in the temperature range 350-500 °C and strain rate range 0.01-1 s^{-1} with efficiency values between 15 and 20% which do not fall into the specific domains. These contours indicate a transient behavior where no stable microstructural mechanism occurs. However, because of the low efficiency (15-20%) and temperature (350-425 °C) inside the region, DRV is one of the active microstructural mechanisms.
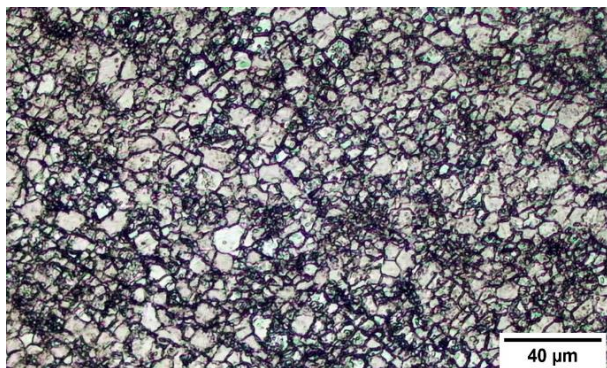

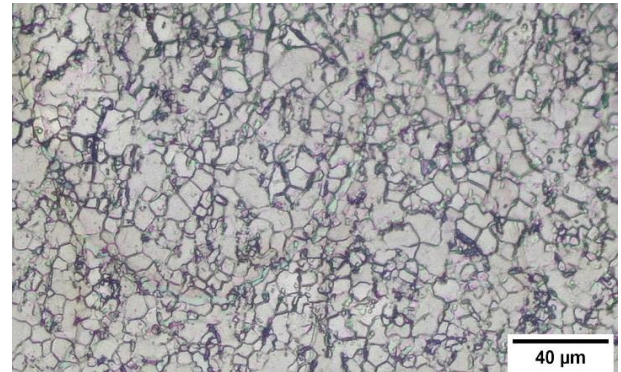**Fig. 6.** Microstructure of sample deformed at 400 °C-0.001s^{-1}.

Fig. 7. Microstructure of sample deformed at 450 °C-1s^{-1}.

Fig. 8. Microstructure of sample deformed at 300 °C-1s^{-1}, where twins and flow localization regions are indicated by red and blue arrows, respectively.

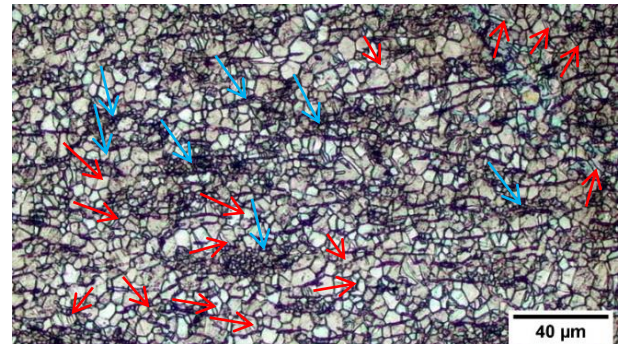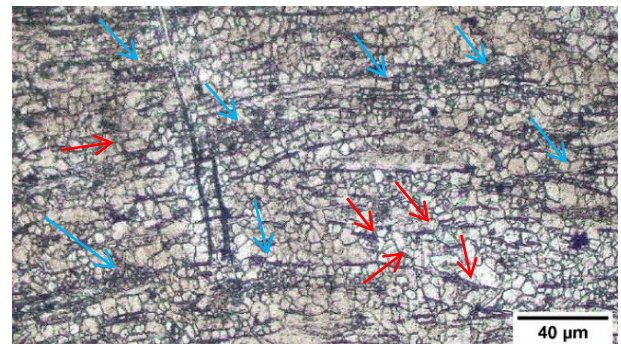**Fig. 9.** Microstructure of sample deformed at 350 °C-0.1s^{-1} where twins and flow localization regions are indicated by red and blue arrows, respectively.

A continuum criterion for the occurrence of flow instability is obtained by utilizing the extremism principles of irreversible thermodynamic to identify the regimes of flow instabilities [47], and given by:

$$\xi(\dot{\varepsilon}) = \frac{\partial \ ln[m/(m+1)]}{\partial \ln \dot{\varepsilon}} + m < 0 \qquad (5)$$

The variation of instability parameter $\xi(\dot{\varepsilon})$ was counted according to Eq.(5) as a function of strain rate and deformation temperature, and used to establish the

instability map. The flow instabilities in hot deformation occur in regimes with negative values of $\xi(\dot{\varepsilon})$. The instability map is superimposed on the power dissipation map to establish a processing map, which exhibits both the flow instabilities' regimes and domains representing various microstructural mechanisms. The constructed instability and power dissipation maps for Mg-5Gd-2.5Nd-0.5Zn-0.5Zr alloy at the strain of 0.3 are shown in Fig. 10.

As can be observed in Fig. 10, the flow instability region consists of the region of high strain rates. The flow instability occurred at strain rates greater than 0.03 s^{-1} and in the temperature range of 300-500 °C. As it was mentioned in section 3.3. samples deformed at 300 °C and different strain rates, and 350 °C -1 s^{-1} failed by cracking following the imposed strain. Considering fracture surface, and microstructures of Mg-5Gd-2.5Nd-0.5Zn-0.5Zr alloy, i.e. Figs. 4, 8 and 9, typical manifestations of the flow instability for the alloy are flow localization bands, cracking, mechanical twinning, and flow rotations.

While DRV, DRX, and superplastic deformation are usually considered as "safe" mechanisms, the efficiency of power dissipation changes with these microstructural processes. Moreover, the dissolution or growth of secondary phases, deformation-induced phase transformation and precipitation under dynamic conditions can affect the efficiency of power dissipation [48].
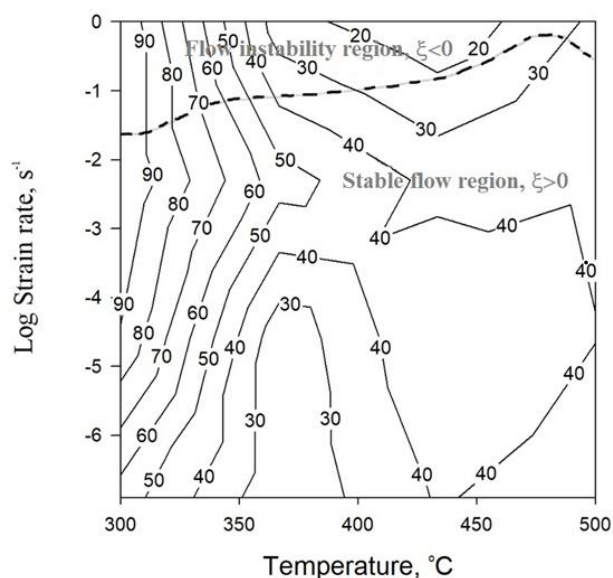
4. Conclusions

The hot workability of Mg-5Gd-0,5Zn-0.5Zr-2.5Nd alloy was studied at temperature ranges of 300 °C to 500 °C and strain rate ranges of 0.001-1s^{-1}. The following facts can be drawn from the analysis.

-True stress-strain curves at low temperature and strain rates range of 0.001-1s^{-1}, show peak stress followed by a continuous decrease in the flow stress. However, at high temperatures and low strain rate, the flow stress reached a steady state.

- The hot deformation of samples at 300 °C, and 350 °C-1s^{-1} failed as a consequence of the initiation and growth of cracks which can be ascribed to the restricted slip deformation at the imposed conditions.

-Dynamic recrystallized grain size was mainly controlled by the RE constituents, temperature and strain rate in which temperature was more effective than strain rate.

-The constructed power dissipation map for Mg-5Gd-0,5Zn-0.5Zr-2.5Nd alloy shows three domains with the peak efficiency of about 90%, 40%, and 30%, namely A, B and C; which occur in the temperature and strain rate ranges of 300- 350 °C/10^{-6}-1 s^{-1} (A), 350- 400 °C /10^{-6}-10^{-3}s^{-1}(B), and 350- 500 °C/10^{-2}-1 s^{-1} (C), respectively. The representative microstructure in domain B and C reveals almost completely recrystallized structures with equiaxed DRX grains and that corresponds to the domain A indicates twins and shear bands.

5. References

[1] S. Jayasathyakawin, M. Ravichandran, N. Baskar, C.A. Chairman, R. Balasundaram, Mechanical properties and applications of Magnesium alloy–Review, *Materials Today: Proceedings* (2020).

[2] Z. Yu, C. Xu, J. Meng, X. Zhang, S. Kamado, Microstructure evolution and mechanical properties of as-extruded Mg-Gd-Y-Zr alloy with Zn and Nd additions, *Materials Science and Engineering: A* 713 (2018) 234-243.

[3] Y. Luo, Y. Wu, Q. Deng, Y. Zhang, J. Chen, L. Peng, Microstructures and mechanical properties of Mg-Gd-Zn-Zr alloys prepared by spark plasma sintering, *Journal of Alloys and Compounds* 820 (2020) 153405.

[4] T. Xu, Y. Yang, X. Peng, J. Song, F. Pan, Overview of advancement and development trend on magnesium alloy, *Journal of Magnesium and Alloys* 7 (3) (2019) 536-544.

[5] A. Arslan Kaya, Fundamentals of Magnesium Alloy Metallurgy, Woodhead Publishing Limited, 2013.

Fig. 10. The processing map of Mg-5Gd-2.5Nd-0.5Zn-0.5Zr alloy, where above the dash line is the flow instability region (ξ<0), and below the dash line represents the stable flow region (ξ>0).

[6] T. Al-Samman, Modification of texture and microstructure of magnesium alloy extrusions by particle-stimulated recrystallization, *Materials Science and Engineering A*-S 560 (2013) 561-566.

[7] L.W.F. Mackenzie, M.O. Pekguleryuz, The recrystallization and texture of magnesium-zinc-cerium alloys, *Scripta Materialia* 59 (2008) 665-668.

[8] S.M. He, X.Q. Zeng, L.M. Peng, X. Gao, J.F. Nie, W.J. Ding, Precipitation in a Mg-10Gd-3Y-0.4Zr (wt.%) alloy during isothermal aging at 250°C, *Journal of Alloys and Compounds* 421(1) (2006) 309-313.

[9] N. Ma, Q. Peng, J. Pan, H. Li, W. Xiao, Effect of microalloying with rare-earth on recrystallization behavior and damping properties of Mg sheets, *Journal of Alloys and Compounds* 592 (2014) 24-34.

[10] L. Gao, R. Chen, E. Han, Effects of rare-earth elements Gd and Y on the solid solution strengthening of Mg alloys, *Journal of Alloys and Compounds* 481(1-2) (2009) 379-384.

[11] J. Gröbner, A. Kozlov, X.Y. Fang, S.M. Zhu, J.F. Nie, M.A. Gibson, R. Schmid-Fetzer, Phase equilibria and transformations in ternary Mg-Gd-Zn alloys, *Acta materialia* 90 (2015) 400-416.

[12] A. Kula, X. Jia, R. K. Mishra, M. Niewczas, Mechanical Properties of Mg-Gd and Mg-Y Solid Solutions, *Metallurgical and Materials Transactions B* 47 (2016) 3333–3342.

[13] J. Liu, L.X. Yang, C.Y. Zhang, B. Zhang, T. Zhang, Y. Li, K.M. Wu, F.H. Wang, Role of the LPSO structure in the improvement of corrosion resistance of Mg-Gd-Zn-Zr alloys, *Journal of Alloys and Compounds* 782 (2019) 648-658.

[14] J. D. Robson, C. Paa-Rai, The interaction of grain refinement and ageing in magnesium-zinc–zirconium (ZK) alloys, *Acta Materialia* 95 (2015) 10-19.

[15] C. Wang, G. Wu, E.J. Lavernia, W. Ding, Influences of heat treatment on microstructural evolution and tensile behavior of squeeze-cast Mg-Gd-Y-Zr alloy, *Journal of Materials Science* 52 (4) (2017) 1831-1846.

[16] T. Honma, T. Ohkubo, S. Kamado, K. Hono, Effect of Zn additions on the age-hardening of Mg-2.0 Gd-1.2 Y-0.2 Zr alloys, *Acta Materialia* 55(12) (2007) 4137-4150.

[17] H. Liu, Y. Chen, Y. Tang, S. Wei, G. Niu, The microstructure, tensile properties, and creep behavior of as-cast Mg (1–10)% Sn alloys, *Journal of Alloys and Compounds* 440 (2007) 122-126.

[18] P. Poddar, K. Sahoo, S. Mukherjee, A.K. Ray, Creep behavior of Mg-8% Sn and Mg-8% Sn-3% Al-1% Si alloys, *Materials Science and Engineering: A* 545 (2012) 103-110.

[19] D.H. Kim, J.Y. Lee, H.K. Lim, J.S. Kyeong, W.T. Kim, D.H. Kim, The effect of microstructure evolution on the elevated temperature mechanical properties in Mg-Sn-Ca system, *Materials Transactions* 49 (2008) 2405-2413.

[20] X. Luo, L. Kang, Q. Li, Y. Chai, Microstructure and hot compression deformation of the as-cast Mg-5.0 Sn-1.5 Y-0.1 Zr alloy, *Applied Physics A* 120(2) (2015) 699-705.

[21] S.H. Park, J.-G. Jung, Y.M. Kim, B.S. You, A new high-strength extruded Mg-8Al-4Sn-2Zn alloy, *Materials Letters* 139 (2015) 35-38.

[22] K. Hantzsche, J. Bohlen, J. Wendt, K.U. Kainer, S.B. Yi, D. Letzig, Effect of rare earth additions on microstructure and texture development of magnesium alloy sheets, *Scripta Materialia* 63 (2010) 725-730.

[23] X. Jin, W. Xu, Z. Yang, C. Yuan, D. Shan, B. Teng, B.C. Jin, Analysis of abnormal texture formation and strengthening mechanism in an extruded Mg-Gd-Y-Zn-Zr alloy, *Journal of Materials Science & Technology* 45 (2020) 133-145.

[24] X. Heng, Y. Zhang, W. Rong, Y. Wu, L. Peng, A super high-strength Mg-Gd-Y-Zn-Mn alloy fabricated by hot extrusion and strain aging, *Materials and Design* 169 (2019) 107666.

[25] J. Zhang, Zh. Kang, F. Wang, Mechanical properties and biocorrosion resistance of the Mg-Gd-Nd-Zn-Zr alloy processed by equal channel angular pressing, *Materials Science and Engineering: C* 68 (2016) 194-197.

[26] X. Xia, Q. Chen, K. Zhang, Z. Zhao, M. Ma, X. Li, Y. Li, Hot deformation behavior and processing map of coarse-grained Mg-Gd-Y-Nd-Zr alloy, *Materials Science and Engineering: A* 587 (2013) 283-290.

[27] Dieter GE Workability testing techniques. American Society for Metals, Ohio, 1984.

[28] R. Ebrahimi, A. Najafizadeh, A new method for evaluation of friction in bulk metal forming, *Journal of Materials Processing Technology* 152 (2004) 136-143.

[29] Z. Zhang, Z. Yan, Y. Du, G. Zhang, J. Zhu, L. Ren, Y. Wang, Hot deformation behavior of homogenized Mg-13.5 Gd-3.2 Y-2.3 Zn-0.5 Zr alloy via hot compression tests, *Materials* 11 (2018) 2282.

[30] L. Li, X. Zhang, Hot compression deformation behavior and processing parameters of a cast Mg-Gd-Y-Zr alloy, *Materials Science and Engineering: A* 528(3) (2011) 1396-1401.

[31] X. Xia, Q. Chen, K. Zhang, Z. Zhao, M. Ma, X. Li, Y. Li, Hot deformation behavior and processing map of coarse-grained Mg-Gd-Y-Nd-Zr alloy, *Materials Science and Engineering: A* 587 (2013) 283-290.

[32] C. Wang, Y. Liu, T. Lin, T. Luo, Y. Zhao, H. Hou, Y. Yang, Hot compression deformation behavior of Mg-5Zn-3.5 Sn-1Mn-0.5 Ca-0.5 Cu alloy, *Materials Characterization* 157 (2019) 109896.

[33] C. Sellars, W. Tegart, Relationship between strength and structure in deformation at elevated temperatures, *Mem Sci Rev Met* 63(9) (1966) 731-745.

[34] M. Aghaie-Khafri, N. Golarzi, Dynamic and metadynamic recrystallization of Hastelloy X superalloy, *Journal of Materials Science* 43 (2008) 3717-3724.

[35] M.H. Barezban, R. Roumina, H. Mirzadeh, R. Mahmudi, Effect of Gd on dynamic recrystallization behavior of

magnesium during hot compression, *Journal of alloys and compounds*, 791 (2019) 1200-1206.

[36] G. Ebrahimi, A.R. Maldar, R. Ebrahimi, A. Davoodi, Effect of thermomechanical parameters on dynamically recrystallized grain size of AZ91 magnesium alloy, *Journal of alloys and compounds* 509(6) (2011) 2703-2708.

[37] Z.Y. Cai, C.j. Che, R.H. Chang, L.R. Cheng, Q.M. Chen, Study on the constitutive behavior and hot deformation characteristic of Mg–4Sm–2Zn–0.5 Zr Alloy, *International Journal of Precision Engineering and Manufacturing*, 20(3) (2019) 407-415.

[38] Prasad, Y., K. Rao, and S. Sasidhar, Hot working guide: a compendium of processing maps, ASM international, 2015.

[39] M. Saadati, R.A. Khosroshahi, G. Ebrahimi, M. Jahazi, Twin-assisted precipitation during hot compression of an Mg-Gd-Zn-Zr magnesium alloy, *Materials Science and Engineering: A* 706 (2017) 142-152.

[40] X.-L. Hou, Y. Li, P. Lv, J. Cai, L. Ji, Q.F. Guan, Hot deformation behavior and microstructure evolution of a Mg-Gd-Nd-Y-Zn alloy, *Rare Metals* 35(7) (2016) 532-536.

[41] S. Anbu Selvan, S. Ramanathan, Hot workability of as-cast and extruded ZE41A magnesium alloy using processing maps, *Transactions of Nonferrous Metals Society of China* 21(2) (2011) 257-264.

[42] Y. Wang, Q. Pan, Y. Song, C. Li, Z. Li, Hot deformation and processing maps of X-750 nickel-based superalloy, *Materials & Design* 51 (2013) 154-160.

[43] M. Aghaie-Khafri, F. Adhami, Hot deformation of 15-5 PH stainless steel, *Materials Science and Engineering: A* 527 (2010) 1052-1057.

[44] C. Sun, G. Liu, Q. Zhang, R. Li, L. Wang, Determination of hot deformation behavior and processing maps of IN 028 alloy using isothermal hot compression test, *Materials Science and Engineering: A* 595 (2014) 92-98.

[45] Y.B. Tan, L.H. Yang, C. Tian, W.C. Liu, R.P. Liu, X.Y. Zhang, Processing maps for hot working of 47Zr-45Ti-5Al-3V alloy, *Materials Science and Engineering: A* 597 (2014) 171-177.

[46] S.V.S. Narayana Murty, B. Nageswara Rao, Development and validation of a processing map for AFNOR 7020 aluminium alloy, Materials Science and Technology 20 (2004) 772-782.

[47] O. Salari, A. Abdi, M. Aghaie-Khafri, A new criterion for construction of instability maps in hot deformation, *Materials Performance and Characterization* 8(5) (2019) 856-868.

[48] E. Pu, W. Zheng, J. Xiang, Z. Song, J. Li, Hot deformation characteristic and processing map of superaustenitic stainless steel S32654, *Materials Science and Engineering: A* 598 (2014) 174-1.